Pullback scheme implementation in ORB5

Alexey Mishchenko[a], Axel Könies, Ralf Kleiber, and Matthias Borchardt
Max Planck Institute for Plasma Physics, D-17491 Greifswald, Germany

Alberto Bottino, Alessandro Biancalani, Roman Hatzky, and Thomas Hayward-Schneider
Max Planck Institute for Plasma Physics, D-85748 Garching, Germany

Noé Ohana, Emmanuel Lanti, Stephan Brunner, and Laurent Villard
Ecolé Polytechnique Fédérale de Lausanne (EPFL),
Swiss Plasma Center (SPC), CH-1015 Lausanne, Switzerland

The pullback scheme is implemented in the global gyrokinetic particle-in-cell code ORB5 [S. Jolliet et al, Comp. Phys. Comm., **177**, 409 (2007)] to mitigate the cancellation problem in electromagnetic simulations. The equations and the discretisation used by the code are described. Numerical simulations of the Toroidal Alfvén Eigenmodes are performed in linear and nonlinear regimes to verify the scheme. A considerable improvement in the code efficiency is observed. For the internal kink mode, it is shown that the pullback mitigation efficiently cures a numerical instability which would make the simulation more costly otherwise.

[a] alexey.mishchenko@ipp.mpg.de

I. INTRODUCTION

Electromagnetic effects are important in fusion plasmas. Alfvén waves, Magneto-Hydro-Dynamic (MHD) activity, electromagnetic modifications of the drift waves and the turbulent transport are well-known examples. In many cases, a combination of the global, electromagnetic and kinetic contributions is essential. Such complexity usually cannot be addressed analytically and calls for a numerical approach, certainly in realistic magnetic geometries under realistic fusion plasma conditions.

Global gyrokinetic particle-in-cell simulations represent such an approach. In this paper we focus on a particular code of this type, ORB5 [1]. This code has been intensively used for gyrokinetic turbulence studies, usually in the electrostatic regime [2]. The electromagnetic simulations have been inhibited by the so-called cancellation problem [3, 4]. In ORB5, this problem has been mitigated using the control variate approach [5]. This mitigation technique has been used for electromagnetic microturbulence simulations [6], and for the simulations of Toroidal Alfvén Eigenmodes [7, 8]. In this paper we describe an implementation in ORB5 of another mitigation scheme, the so-called pullback mitigation [9–12]. This approach can be used in combination with the control variate scheme [5]. As a consequence, the code efficiency improves considerably. Previously, the pullback mitigation has been implemented in the EUTERPE code [10–14]. An alternative approach to the cancellation mitigation has been recently proposed for the GTC [15, 16].

In our simulations, we consider the Toroidal Alfvén Eigenmodes [17, 18] destabilised by the fast particles [19, 20] and the internal kink instability [21] in tokamak geometry. To our knowledge, this is the first time the internal kink instability has been simulated using the global gyrokinetic particle-in-cell code in tokamak geometry at a realistic value of plasma β. For simulations in straight tokamak, see Refs. [22–24].

The paper is organised as follows. In Sec. II, the equations solved by ORB5 are presented. In Sec. III, the discretisation used by the code is discussed. Simulations using the newly implemented schemes are presented in Sec. IV. Conclusions are made in Sec. V.

II. EQUATIONS SOLVED BY ORB5

The global gyrokinetic particle-in-cell code ORB5 [1] solves the gyrokinetic Vlasov-Maxwell system of equations [25]. The species distribution function f_s is split into the "background" control variate F_{0s} and the time-dependent deviation from the control variate δf_s so that $f_s = F_{0s} + \delta f_s$. Here, the subscript $s = \mathrm{i}, \mathrm{e}, \mathrm{f}$ indicates the particle species (bulk plasma ions and electrons, fast particles). The control variate is usually chosen to be a Maxwellian. The deviation from the control variate δf_s is found from the gyrokinetic Vlasov equation:

$$\frac{\partial \delta f_s}{\partial t} + \dot{\boldsymbol{R}} \cdot \frac{\partial \delta f_s}{\partial \boldsymbol{R}}\Big|_{v_\parallel} + \dot{v}_\parallel \frac{\partial \delta f_s}{\partial v_\parallel} = -\dot{\boldsymbol{R}}^{(1)} \cdot \frac{\partial F_{0s}}{\partial \boldsymbol{R}}\Big|_{\varepsilon} - \dot{\varepsilon}^{(1)} \frac{\partial F_{0s}}{\partial \varepsilon} \tag{1}$$

Here, $[\dot{\boldsymbol{R}}, \dot{v}_\parallel]$ correspond to the gyrocenter trajectories with $[\dot{\boldsymbol{R}}^{(1)}, \dot{\varepsilon}_\parallel^{(1)}]$ the perturbations of the trajectories proportional to the field fluctuations. Note that the spatial derivative at the right hand side of Eq. (1) is taken at a constant energy $\varepsilon = v_\parallel^2/2 + \mu B$ whereas the spatial derivative on the left hand side of Eq. (1) is taken at a constant parallel velocity $v_\parallel$. Here, $\mu = v_\perp^2/(2B)$ is the magnetic moment. The mixed-variable [10] perturbed equations of motion are

$$\dot{\boldsymbol{R}}^{(1)} = \frac{\boldsymbol{b}}{B_\parallel^*} \times \nabla \Big\langle \phi - v_\parallel A_\parallel^{(\mathrm{s})} - v_\parallel A_\parallel^{(\mathrm{h})} \Big\rangle - \frac{q_s}{m_s} \langle A_\parallel^{(\mathrm{h})} \rangle \, \boldsymbol{b}^* \tag{2}$$

$$\dot{v}_\parallel^{(1)} = -\frac{q_s}{m_s} \left[\boldsymbol{b}^* \cdot \nabla \Big\langle \phi - v_\parallel A_\parallel^{(\mathrm{h})} \Big\rangle + \frac{\partial}{\partial t} \Big\langle A_\parallel^{(\mathrm{s})} \Big\rangle \right] - \mu \frac{\boldsymbol{b} \times \nabla B}{B_\parallel^*} \cdot \nabla \Big\langle A_\parallel^{(\mathrm{s})} \Big\rangle \tag{3}$$

Here, ϕ is the perturbed electrostatic potential, $A_\parallel^{(\mathrm{h})}$ and $A_\parallel^{(\mathrm{s})}$ are the Hamiltonian and the symplectic parts [10] of the perturbed magnetic potential, m_s is the mass of the particle, $B_\parallel^* = \boldsymbol{b} \cdot \nabla \times \boldsymbol{A}^*$, $\boldsymbol{b}^* = \nabla \times \boldsymbol{A}^*/B_\parallel^*$, $\boldsymbol{A}^* = \boldsymbol{A} + (m_s v_\parallel/q_s)\boldsymbol{b}$ is the modified vector potential, $\boldsymbol{A}$ is the magnetic potential corresponding to the equilibrium magnetic field, $\boldsymbol{B} = \nabla \times \boldsymbol{A}$, $\boldsymbol{b} = \boldsymbol{B}/B$ is the unit vector in the direction of the equilibrium magnetic field, and the gyro-averaged potential is defined as usual $\langle \phi \rangle = \oint \phi(\boldsymbol{R} + \boldsymbol{\rho}) \mathrm{d}\alpha/(2\pi)$ with $\boldsymbol{\rho}$ the gyroradius of the particle and α the gyro-phase. Note that some nonlinear terms [11] are not included in Eq. (3). These terms will be considered in Sec. IV C.

The perturbed electrostatic potential is found from the gyrokinetic quasineutrality equation:

$$-\nabla \cdot \left[\left(\sum_{s=\mathrm{i,f}} \frac{q_s^2 n_s}{T_s} \rho_s^2 \right) \nabla_\perp \phi \right] = \sum_{s=\mathrm{i,e,f}} q_s n_{1s} \tag{4}$$

where $n_{1s} = \int \mathrm{d}^6 Z\, \delta f_s\, \delta(\boldsymbol{R}+\boldsymbol{\rho}-\boldsymbol{x})$ is the perturbed gyrocenter density, $\rho_s = \sqrt{m_s T_s}/(q_s B)$ is the thermal gyroradius, q_s is the charge of the particle, and $\mathrm{d}^6 Z = B_\parallel^*\, \mathrm{d}\boldsymbol{R}\, \mathrm{d}v_\parallel\, \mathrm{d}\mu\, \mathrm{d}\alpha$ is the phase-space volume. The polarization density is treated in the long-wavelength approximation and finite Larmor radius (FLR) effects are neglected for electrons. The zeroth-order densities of the particle species satisfy the quasineutrality equation $\sum_s q_s n_{0s} = 0$ with $s = \mathrm{i}, \mathrm{e}, \mathrm{f}$.

The perturbed energy evolves according to the equation:

$$\dot{\varepsilon}^{(1)} = v_\parallel \dot{v}_\parallel^{(1)} + \mu \dot{\boldsymbol{R}}^{(1)} \cdot \nabla B = -\frac{q_s}{m_s}\left[m_s \mu \frac{\boldsymbol{b}\times\nabla B}{q_s B_\parallel^*} + \frac{m_s v_\parallel^2}{q_s B_\parallel^*}(\nabla\times\boldsymbol{b})\right]\cdot\nabla\langle\phi\rangle + \tag{5}$$
$$+ \frac{q_s}{m_s} v_\parallel \left[v_\parallel \boldsymbol{b} + m_s \mu \frac{\boldsymbol{b}\times\nabla B}{q_s B_\parallel^*} + \frac{m_s v_\parallel^2}{q_s B_\parallel^*}(\nabla\times\boldsymbol{b})\right]\cdot\nabla\langle A_\parallel^{(\mathrm{h})}\rangle + \frac{q_s}{m_s}\mu B\left[\nabla\cdot\boldsymbol{b} - \frac{m v_\parallel}{q B_\parallel^*}\frac{\nabla\times\boldsymbol{B}}{B^2}\cdot\nabla B\right]\left\langle A_\parallel^{(\mathrm{h})}\right\rangle$$

The symplectic part $A_\parallel^{(\mathrm{s})}$ of the perturbed magnetic potential is found [10] from the equation:

$$\frac{\partial}{\partial t} A_\parallel^{(\mathrm{s})} + \boldsymbol{b}\cdot\nabla\phi = 0 \tag{6}$$

For the Hamiltonian part $A_\parallel^{(\mathrm{h})}$, the mixed-variable parallel Ampere's law is solved:

$$\left(\sum_{s=\mathrm{i,e,f}} \frac{\beta_s}{\rho_s^2} - \nabla_\perp^2\right) A_\parallel^{(\mathrm{h})} = \mu_0 \sum_{s=\mathrm{i,e,f}} j_{\parallel 1s} + \nabla_\perp^2 A_\parallel^{(\mathrm{s})} \tag{7}$$

with $j_{\parallel 1s} = \int \mathrm{d}^6 Z\, v_\parallel \delta f_s\, \delta(\boldsymbol{R}+\boldsymbol{\rho}-\boldsymbol{x})$ the perturbed parallel gyrocenter current.

The equations are solved employing the mixed-variable pullback algorithm [10]:

1. At the end of each time step, redefine the magnetic potential splitting, so that the entire instantaneous value of the parallel magnetic potential $A_\parallel(t_i)$ is collected in its 'symplectic part':

$$A_{\parallel(\mathrm{new})}^{(\mathrm{s})}(t_i) = A_\parallel(t_i) = A_{\parallel(\mathrm{old})}^{(\mathrm{s})}(t_i) + A_{\parallel(\mathrm{old})}^{(\mathrm{h})}(t_i) \tag{8}$$

2. As a consequence of the new splitting, Eq. (8), the 'Hamiltonian' part of the vector potential must be corrected:

$$A_{\parallel(\mathrm{new})}^{(\mathrm{h})}(t_i) = 0 \tag{9}$$

3. For this modified splitting, the new mixed-variable distribution function must coincide with its symplectic-formulation counterpart. The symplectic-formulation distribution function is independent on the way of splitting and can be found invoking the pullback and using the old values of the mixed-variable distribution function and the 'Hamiltonian' part of the parallel vector potential found solving, respectively, the gyrokinetic equation and Ampere's law, Eq. (7), at the current time step t_i:

$$\delta f_{s(\mathrm{new})}^{(\mathrm{m})}(t_i) = \delta f_s^{(\mathrm{s})}(t_i) = \delta f_{s(\mathrm{old})}^{(\mathrm{m})}(t_i) + \frac{q_s\,\langle A_{\parallel(\mathrm{old})}^{(\mathrm{h})}(t_i)\rangle}{m_s}\frac{\partial F_{0s}}{\partial v_\parallel} \tag{10}$$

   Note here that Eq. (10) corresponds to the linearised version of the pullback transformation. In the fully nonlinear case [11], the orbits of the markers must be transformed with the marker weights kept fixed during the transformation. This approach will be considered in Sec. IV C.

4. Proceed, explicitly solving the mixed-variable system of Eqs. (2)–(7) at the next time step $t_i + \Delta t$ in a usual way, but using Eqs. (8)–(10) as the initial conditions.

This algorithm combined with the usual control variate [5] is the key technique mitigating the cancellation problem [3] in the electromagnetic gyrokinetic simulations using ORB5.

It is important to check the energy conservation in simulations. This may be a complication since, in ORB5, the energy is monitored in the Hamiltonian ($p_\parallel$) coordinates whereas the gyrocenter markers are pushed in the mixed-variable phase space. The evolution of the kinetic energy and the definition of the field energy depend on the

phase-space coordinates used to define the gyrocenters since this definition includes field terms. To overcome this complication in ORB5, we transform the mixed-variable distribution function into the Hamiltonian coordinates:

$$\delta f_s^{(\mathrm{h})}(t_i) = \delta f_s^{(\mathrm{m})}(t_i) - \frac{q_s \langle A_\parallel^{(\mathrm{s})}(t_i)\rangle}{m_s} \frac{\partial F_{0s}}{\partial v_\parallel} \tag{11}$$

We can use then $\delta f_s^{(\mathrm{h})}$ to compute the particle energy transfer in the usual way [26, 27]. For the electromagnetic energy, we transform the mixed-variable perturbed parallel current into the Hamiltonian-variable parallel current:

$$\mu_0 j_{\parallel 1\mathrm{e}}^{(\mathrm{h})} = \mu_0 j_{\parallel 1\mathrm{e}}^{(\mathrm{m})} + \frac{\beta_\mathrm{e}}{\rho_\mathrm{e}^2} A_\parallel^{(\mathrm{s})} \tag{12}$$

In this paper, we transform only the electron perturbed current since the corresponding correction for ions is much smaller, implying $j_{\parallel 1i}^{(\mathrm{h})} \approx j_{\parallel 1i}^{(\mathrm{m})}$. The perturbed gyrocenter density does not need to be transformed, $n_{\parallel 1s}^{(\mathrm{h})} = n_{\parallel 1s}^{(\mathrm{m})}$, if the background distribution function is a Maxwellian. The perturbed field energy is then defined in the usual way:

$$W_{(\mathrm{field})} = \frac{1}{2} \sum_{s=\mathrm{i,e}} \left(n_{1s}^{(\mathrm{h})} \phi - j_{\parallel 1s}^{(\mathrm{h})} A_\parallel \right) \ , \quad A_\parallel = A_\parallel^{(\mathrm{h})} + A_\parallel^{(\mathrm{s})} \tag{13}$$

These transformations of the distribution function, Eq. (11) and of the current, Eq. (12), are applied only for the energy diagnostics and do not disturb the simulation itself.

III. DISCRETISATION

The deviation of the distribution function f_s from the control variate F_{0s} is discretised in the mixed variable [9, 10] with markers. This discretisation can formally be written as

$$\delta f_s^{(\mathrm{m})}(\boldsymbol{R}, v_\parallel, \mu, t) = \sum_{\nu=1}^{N_\mathrm{p}} w_{s\nu}(t) \delta(\boldsymbol{R} - \boldsymbol{R}_\nu) \delta(v_\parallel - v_{\nu\parallel}) \delta(\mu - \mu_\nu) \ , \tag{14}$$

where N_p is the number of markers, $(\boldsymbol{R}_\nu, v_{\nu\parallel}, \mu_\nu)$ are the marker phase space coordinates and $w_{s\nu}$ is the weight of a marker. The markers move along the gyrocenter orbits. The evolution of the marker weights $w_{s\nu}(t)$ is given by the gyrokinetic equation (1). An alternative to this is to use the Lagrange invariance of the full distribution function f_s along the gyrocenter orbits [1]. The pullback step in the algorithm described above modifies the marker weights according to Eq. (10) at the end of each time steps. The marker positions do not change during this operation.

The perturbed potentials are discretized with the finite-element method

$$\phi(\boldsymbol{x}, t) = \sum_{\widetilde{L}}^{N_\mathrm{FE}} \phi_{\widetilde{L}}(t) \widetilde{\Lambda}_{\widetilde{L}}(\boldsymbol{x}) \ , \quad A_\parallel^{(\mathrm{s})}(\boldsymbol{x}, t) = \sum_{\widetilde{L}}^{N_\mathrm{FE}} a_{\widetilde{L}}^{(\mathrm{s})}(t) \widetilde{\Lambda}_{\widetilde{L}}(\boldsymbol{x}) \ , \quad A_\parallel^{(\mathrm{h})}(\boldsymbol{x}, t) = \sum_{\widetilde{L}}^{N_\mathrm{FE}} a_{\widetilde{L}}^{(\mathrm{h})}(t) \widetilde{\Lambda}_{\widetilde{L}}(\boldsymbol{x}) \tag{15}$$

with $\widetilde{\Lambda}_{\widetilde{L}}(\boldsymbol{x})$ the finite elements (tensor product of B splines, see below); N_FE the total number of the finite elements; $\phi_{\widetilde{L}}$, $a_{\widetilde{L}}^{(\mathrm{s})}$ and $a_{\widetilde{L}}^{(\mathrm{h})}$ the spline coefficients. In the weak formulation, the field equations (4), (6) and (7) become the linear algebra equations in this discretisation with the differential operators represented by the matrices. Thus, Eq. (6) for $A_\parallel^{(\mathrm{s})}$ becomes

$$\sum_{\widetilde{L}}^{N_\mathrm{FE}} B_{\widetilde{K}\widetilde{L}} \frac{\mathrm{d}a_{\widetilde{L}}^{(\mathrm{s})}}{\mathrm{d}t} = \sum_{\widetilde{R}}^{N_\mathrm{FE}} M_{\widetilde{K}\widetilde{R}}^{(\mathrm{I})} \phi_{\widetilde{R}} \tag{16}$$

with the mass matrix $B_{\widetilde{K}\widetilde{L}}$ and the matrix $M_{\widetilde{K}\widetilde{L}}^{(\mathrm{I})}$ representing the parallel derivative:

$$B_{\widetilde{K}\widetilde{L}} = \int \mathrm{d}^3x \widetilde{\Lambda}_{\widetilde{K}} \widetilde{\Lambda}_{\widetilde{L}} \ , \quad M_{\widetilde{K}\widetilde{L}}^{(\mathrm{I})} = -\int \mathrm{d}^3x \widetilde{\Lambda}_{\widetilde{K}} \boldsymbol{b} \cdot \nabla \widetilde{\Lambda}_{\widetilde{L}} \tag{17}$$

where $\mathrm{d}^3x = J \, \mathrm{d}s \, \mathrm{d}\theta \, \mathrm{d}\varphi$, $J(s, \theta)$ is the real-space Jacobian, $s = \sqrt{\psi/\psi_\mathrm{a}}$ is the flux label, ψ is the poloidal magnetic flux, ψ_a is the poloidal magnetic flux at the plasma edge, θ is the poloidal angle, and φ is the toroidal angle.

Similarly, the term $\nabla_\perp^2 A_\parallel^{(\mathrm{s})}$ appearing on the right hand side of the parallel Ampere's law, Eq. (7), is discretised in the finite-element representation with a matrix as follows:

$$\nabla_\perp^2 A_\parallel^{(\mathrm{s})} \longrightarrow \sum_{\widetilde{L}}^{N_{\mathrm{FE}}} M^{(\mathrm{II})}_{\widetilde{K}\widetilde{L}} a^{(\mathrm{s})}_{\widetilde{l}}(t)\ ,\ \ M^{(\mathrm{II})}_{\widetilde{K}\widetilde{L}} = -\int_\Omega \mathrm{d}^3x \nabla_\perp \widetilde{\Lambda}_{\widetilde{K}} \cdot \nabla_\perp \widetilde{\Lambda}_{\widetilde{L}} + \int_{\partial\Omega} \mathrm{d}^2\sigma \cdot \widetilde{\Lambda}_{\widetilde{K}} \nabla_\perp \widetilde{\Lambda}_{\widetilde{L}} \tag{18}$$

where the second term is a boundary integral coming from integration by parts. This trick allows to use linear finite elements, whose second derivatives are singular. For this Laplace matrix, the poloidal-plane approximation for $\nabla_\perp$ can be used. In this case, it can be treated in the same way as the Laplacian appearing on the left hand side of Ampere's law, Eq. (7), with the only difference that $M^{(\mathrm{II})}_{\widetilde{K}\widetilde{L}}$ is used for the multiplication and does not need, therefore, to be inverted.

The treatment of the parallel-derivative matrix $M^{(\mathrm{I})}_{\widetilde{k}\widetilde{l}}$ is more complicated. This matrix must be split into two parts corresponding to the poloidal derivative and the toroidal derivative:

$$M^{(\mathrm{I})}_{\widetilde{K}\widetilde{L}} = -\int \boldsymbol{b}\cdot\nabla\theta\ \widetilde{\Lambda}_{\widetilde{K}} \frac{\partial \widetilde{\Lambda}_{\widetilde{L}}}{\partial\theta}\,\mathrm{d}^3x - \int \boldsymbol{b}\cdot\nabla\varphi\ \widetilde{\Lambda}_{\widetilde{K}} \frac{\partial \widetilde{\Lambda}_{\widetilde{L}}}{\partial\varphi}\,\mathrm{d}^3x \tag{19}$$

These two "poloidal" and "toroidal" matrices have to be treated separately due to the toroidal Fourier transform applied in ORB5 [1, 28] to solve the field Eqs. (4), (6) and (7). Recall that ORB5 solves the gyrokinetic system of equations in an axisymmetric tokamak geometry where the equilibrium does not depend on the toroidal angle φ.

In the three-dimensional space, one defines the finite elements $\widetilde{\Lambda}_{\widetilde{L}}$ as the tensor products of the usual B splines $\lambda_j(x)$, typically cubic:

$$\widetilde{\Lambda}_{\widetilde{L}}(\boldsymbol{x}) = \lambda_j(s)\lambda_k(\theta)\lambda_l(\varphi) \tag{20}$$

Note that we use capital symbols and the tilde notation throughout this paper in order to indicate the tensor-product nature of both the finite elements $\widetilde{\Lambda}_{\widetilde{L}}$ and their indexes $\widetilde{L}$ evident from Eq. (20). The integer indexes j, k, and l of the one-dimensional B splines change from zero to the number of the B splines used in the respective direction. The perturbed field, for example the electrostatic potential ϕ, can be represented in terms of the usual B splines as follows

$$\phi(s,\theta,\varphi) = \sum_{l'=0}^{N_\varphi-1} \sum_{j'k'} \phi_{j'k'l'} \lambda_{j'}(s)\lambda_{k'}(\theta)\lambda_{l'}(\varphi) \tag{21}$$

with N_φ being the number of the toroidal B splines. The spline coefficients $\phi_{j'k'l'}$ can be Fourier transformed in the toroidal coordinate. The Fast-Fourier-Transform is used in ORB5 [28]:

$$\phi_{j'k'l'} = \sum_{n=0}^{N_\varphi-1} \phi^{(n)}_{j'k'}\ \exp\left[\frac{2\pi\mathrm{i}}{N_\varphi}\, nl'\right] \tag{22}$$

Using this representation, one can write for the toroidal derivative

$$\frac{\partial\phi(s,\theta,\varphi)}{\partial\varphi} = \sum_{l'=0}^{N_\varphi-1} \sum_{n=0}^{N_\varphi-1} \exp\left[\frac{2\pi\mathrm{i}}{N_\varphi}\, nl'\right] \frac{\partial\lambda_{l'}(\varphi)}{\partial\varphi} \sum_{j'k'} \phi^{(n)}_{j'k'} \lambda_{j'}(s)\lambda_{k'}(\theta) \tag{23}$$

In the weak formulation, the finite-element representation of the operator $\partial/\partial\varphi$ acting on the perturbed field ϕ and its toroidal Fourier transform are represented by the tensors B_{jkl} and $B^{(n)}_{jk}$ as follows:

$$B_{jkl} = \int \frac{\partial\phi(s,\theta,\varphi)}{\partial\varphi} \lambda_j(s)\lambda_k(\theta)\lambda_l(\varphi)\, J(s,\theta)\,\mathrm{d}s\,\mathrm{d}\theta\,\mathrm{d}\varphi = \sum_{n=0}^{N_\varphi-1} B^{(n)}_{jk}\ \exp\left[\frac{2\pi\mathrm{i}}{N_\varphi}\, nl\right] \tag{24}$$

Here, the indexes j, k, l and n are integers. Substituting Eq. (23), we can write

$$B_{jkl} = \sum_{l'=0}^{N_\varphi-1} \sum_{n=0}^{N_\varphi-1} \exp\left[\frac{2\pi\mathrm{i}}{N_\varphi}\, nl'\right] \int_0^{2\pi} \frac{\partial\lambda_{l'}(\varphi)}{\partial\varphi}\, \lambda_l(\varphi)\,\mathrm{d}\varphi \sum_{j'k'} \phi^{(n)}_{j'k'} \int \lambda_{j'}(s)\lambda_{k'}(\theta)\lambda_j(s)\lambda_k(\theta)\, J(s,\theta)\,\mathrm{d}s\,\mathrm{d}\theta$$

For the Fourier coefficients $B_{jk}^{(n)}$, we obtain:

$$\sum_{n=0}^{N_\varphi-1} B_{jk}^{(n)} \, \exp\left[\frac{2\pi \mathrm{i}}{N_\varphi} \, nl\right] = \sum_{n=0}^{N_\varphi-1} D^{(n)} \exp\left[\frac{2\pi \mathrm{i}}{N_\varphi} \, nl\right] \sum_{j'k'} \phi_{j'k'}^{(n)} \int \lambda_{j'}(s)\lambda_{k'}(\theta)\lambda_j(s)\lambda_k(\theta) \, J(s,\theta) \, \mathrm{d}s \, \mathrm{d}\theta$$

Thus for the individual toroidal modes, we have to compute

$$B_{jk}^{(n)} = D^{(n)} \sum_{j'k'} \phi_{j'k'}^{(n)} \int \lambda_{j'}(s)\lambda_{k'}(\theta)\lambda_j(s)\lambda_k(\theta) \, J(s,\theta) \, \mathrm{d}s \, \mathrm{d}\theta \tag{25}$$

One sees that the Fourier transform of the toroidal derivative acting on the perturbed electrostatic potential ϕ is constructed from the Fourier transform of the spline coefficients $\phi_{j'k'}^{(n)}$, the two-dimensional mass matrix

$$\int \lambda_{j'}(s)\lambda_{k'}(\theta)\lambda_j(s)\lambda_k(\theta) \, J(s,\theta) \, \mathrm{d}s \, \mathrm{d}\theta \tag{26}$$

and the quantity $D^{(n)}$ defined by

$$D^{(n)} \exp\left[\frac{2\pi \mathrm{i}}{N_\varphi} \, nl\right] = \sum_{l'=0}^{N_\varphi-1} \int_0^{2\pi} \mathrm{d}\varphi \, \frac{\mathrm{d}\lambda_{l'}(\varphi)}{\mathrm{d}\varphi} \, \lambda_l(\varphi) \, \exp\left[\frac{2\pi \mathrm{i}}{N_\varphi} \, nl'\right] \; = \tag{27}$$

$$= \; \exp\left[\frac{2\pi \mathrm{i}}{N_\varphi} \, nl\right] \sum_{k=-p}^{p} \int_0^{2\pi} \mathrm{d}\varphi \, \frac{\mathrm{d}\lambda_{l+k}(\varphi)}{\mathrm{d}\varphi} \, \lambda_l(\varphi) \, \exp\left[\frac{2\pi \mathrm{i}}{N_\varphi} \, nk\right]$$

Here, p is the order of the B splines. Using the periodicity and the symmetry relations for the B splines and their derivatives:

$$\int_0^{2\pi} \lambda_l(\varphi) \, \frac{\partial \lambda_l}{\partial \varphi} \, \mathrm{d}\varphi = 0 \; , \;\; \lambda(x) = \lambda(-x) \; , \quad \lambda'(x) = \, -\lambda'(-x) \; , \;\; \lambda'(x) = \frac{\mathrm{d}\lambda(x)}{\mathrm{d}x}$$

and introducing the notation $\varphi = (2\pi/N_\varphi) \, x$, we can write

$$D^{(n)} = 2\mathrm{i} \sum_{k=1}^{p} \sin\left[\frac{2\pi}{N_\varphi} \, nk\right] \int_0^{2\pi} \frac{\mathrm{d}\lambda_{l+k}(\varphi)}{\mathrm{d}\varphi} \, \lambda_l(\varphi) \, \mathrm{d}\varphi = 2\mathrm{i} \sum_{k=1}^{p} d_k \, \sin\left[\frac{2\pi}{N_\varphi} \, nk\right] \tag{28}$$

Here, we have introduced the notations:

$$d_k = \int_0^{N_\varphi} \frac{\mathrm{d}\lambda_{l+k}(x)}{\mathrm{d}x} \, \lambda_l(x) \, \mathrm{d}x = \sum_{j=0}^{p-k} \int_0^1 \frac{\mathrm{d}P_{j+k}^{(p)}(x)}{\mathrm{d}x} \, P_j^{(p)}(x) \, \mathrm{d}x \; ; \;\; k = 1, \ldots, p \tag{29}$$

with $P_j^{(p)}$ the B spline polynomials of the degree p defined within a grid cell [29]. Summarising, we obtain:

$$D^{(n)} = 2\mathrm{i} \sum_{k=1}^{p} d_k \sin\left(\frac{2\pi}{N_\varphi} \, nk\right) \; , \;\; d_k = \sum_{j=0}^{p-k} \int_0^1 P_j^{(p)}(x) \, \frac{\mathrm{d}P_{j+k}^{(p)}(x)}{\mathrm{d}x} \, \mathrm{d}x \tag{30}$$

For the linear B splines, $p = 1$, we obtain

$$d_1 = \, -\frac{1}{2} \; , \;\; D^{(n)} = \, -\mathrm{i} \, \sin\left(\frac{2\pi n}{N_\varphi}\right) \tag{31}$$

For the quadratic ($p = 2$) B splines:

$$d_1 = \, -\frac{5}{12} \; , \;\; d_2 = \, -\frac{1}{24} \; , \;\; D^{(n)} = \mathrm{i} \sin\left(\frac{2\pi n}{N_\varphi}\right) \left[-\frac{5}{6} - \frac{1}{6} \cos\left(\frac{2\pi n}{N_\varphi}\right)\right] \tag{32}$$

Finally, for the cubic ($p = 3$) B splines:

$$d_1 = -\frac{49}{144}\ ,\ \ d_2 = -\frac{7}{90}\ ,\ \ d_3 = -\frac{1}{720}\ ,\ \ D^{(n)} = \mathrm{i}\sin\left(\frac{2\pi n}{N_\varphi}\right)\left[-\frac{61}{90} - \frac{14}{45}\cos\left(\frac{2\pi n}{N_\varphi}\right) - \frac{1}{90}\cos^2\left(\frac{2\pi n}{N_\varphi}\right)\right] \tag{33}$$

The poloidal derivative in the finite-element toroidal Fourier representation must be treated differently:

$$\frac{\partial\phi(s,\theta,\varphi)}{\partial\theta} = \sum_{l'=0}^{N_\varphi-1}\sum_{n=0}^{N_\varphi-1}\exp\left[\frac{2\pi\mathrm{i}}{N_\varphi}\,nl'\right]\,\lambda_{l'}(\varphi)\sum_{j'k'}\phi^{(n)}_{j'k'}\lambda_{j'}(s)\frac{\partial\lambda_{k'}(\theta)}{\partial\theta} \tag{34}$$

In the weak formulation, the operator $\partial/\partial\theta$ acting of $\phi(\boldsymbol{x})$, represented by the tensors G_{jkl} and $G^{(n)}_{jk}$, is

$$G_{jkl} = \int\frac{\partial\phi(s,\theta,\varphi)}{\partial\theta}\lambda_j(s)\lambda_k(\theta)\lambda_l(\varphi)\,\mathrm{d}s\,\mathrm{d}\theta\,\mathrm{d}\varphi = \sum_{n=0}^{N_\varphi-1}G^{(n)}_{jk}\,\exp\left[\frac{2\pi\mathrm{i}}{N_\varphi}\,nl\right] \tag{35}$$

Performing the same manipulations, as above, we obtain

$$G^{(n)}_{jk} = M^{(n)}\sum_{j'k'}\phi^{(n)}_{j'k'}\int\lambda_{j'}(s)\frac{\partial\lambda_{k'}(\theta)}{\partial\theta}\lambda_j(s)\lambda_k(\theta)\,J(s,\theta)\,\mathrm{d}s\,\mathrm{d}\theta \tag{36}$$

One sees that the Fourier transform of the *poloidal derivative* acting on the perturbed electrostatic potential $\phi(\boldsymbol{x})$ is constructed from the Fourier transform of the spline coefficients $\phi^{(n)}_{j'k'}$, the two-dimensional non-symmetric matrix

$$\int\lambda_{j'}(s)\frac{\partial\lambda_{k'}(\theta)}{\partial\theta}\lambda_j(s)\lambda_k(\theta)\,J(s,\theta)\,\mathrm{d}s\,\mathrm{d}\theta \tag{37}$$

and the new normalisation factors $M^{(n)}$ defined by

$$M^{(n)} = \frac{2\pi}{N_\varphi}\left\{2\sum_{k=1}^{p}c_k\cos\left(\frac{2\pi}{N_\varphi}nk\right) + c_0\right\}\ ,\ \ c_k = \sum_{j=0}^{p-k}\int_0^1\mathrm{d}x P^{(p)}_j(x)P^{(p)}_{j+k}(x) \tag{38}$$

Note the dependence on the toroidal mode number for the normalisation factors $M^{(n)}$ and $D^{(n)}$. The factor $D^{(n)}$ appears in the matrices discretising the toroidal derivative operator. The factor $M^{(n)}$ is needed in the poloidal derivative but also in all other operators which do not involve $\partial/\partial\varphi$. The peculiarity of the poloidal derivative operator is that it leads to non-symmetric matrices. All other matrices used in ORB5 are symmetric.

In explicit terms, the matrix acting on the electrostatic potential in the equation for $A^{(\mathrm{s})}_\parallel$, Eq. (16), is given by

$$\sum_{\widetilde{L}}^{N_{\mathrm{FE}}}M^{(\mathrm{I})}_{\widetilde{K}\widetilde{L}}\phi_{\widetilde{L}} = \sum_{n=0}^{N_\varphi-1}\exp\left[\frac{2\pi\mathrm{i}}{N_\varphi}\,nl\right]\left[M^{(n)}\sum_{j'k'}M^{(\mathrm{I};\theta)}_{jk;j'k'}\phi^{(n)}_{j'k'} + D^{(n)}\sum_{j'k'}M^{(\mathrm{I};\varphi)}_{jk;j'k'}\phi^{(n)}_{j'k'}\right] \tag{39}$$

with the two-dimensional matrices

$$M^{(\mathrm{I};\theta)}_{jk;j'k'} = -\int\boldsymbol{b}\cdot\nabla\theta\ \lambda_{j'}(s)\frac{\partial\lambda_{k'}(\theta)}{\partial\theta}\lambda_j(s)\lambda_k(\theta)\,J(s,\theta)\,\mathrm{d}s\,\mathrm{d}\theta \tag{40}$$

$$M^{(\mathrm{I};\varphi)}_{jk;j'k'} = -\int\boldsymbol{b}\cdot\nabla\varphi\ \lambda_{j'}(s)\lambda_{k'}(\theta)\lambda_j(s)\lambda_k(\theta)\,J(s,\theta)\,\mathrm{d}s\,\mathrm{d}\theta \tag{41}$$

Precisely these expressions have been implemented in ORB5. The field equations are solved for each toroidal mode individually [28]. The matrix routines have been modified in ORB5 to allow for the non-symmetric matrices.

IV. SIMULATIONS

A. Toroidal Alfvén Eigenmode

For verification of the scheme newly implemented in ORB5, we consider the reference case of the international cross-code "ITPA-TAE" benchmark [19, 20]. In this benchmark, the Toroidal Alfvén Eigenmode with the toroidal

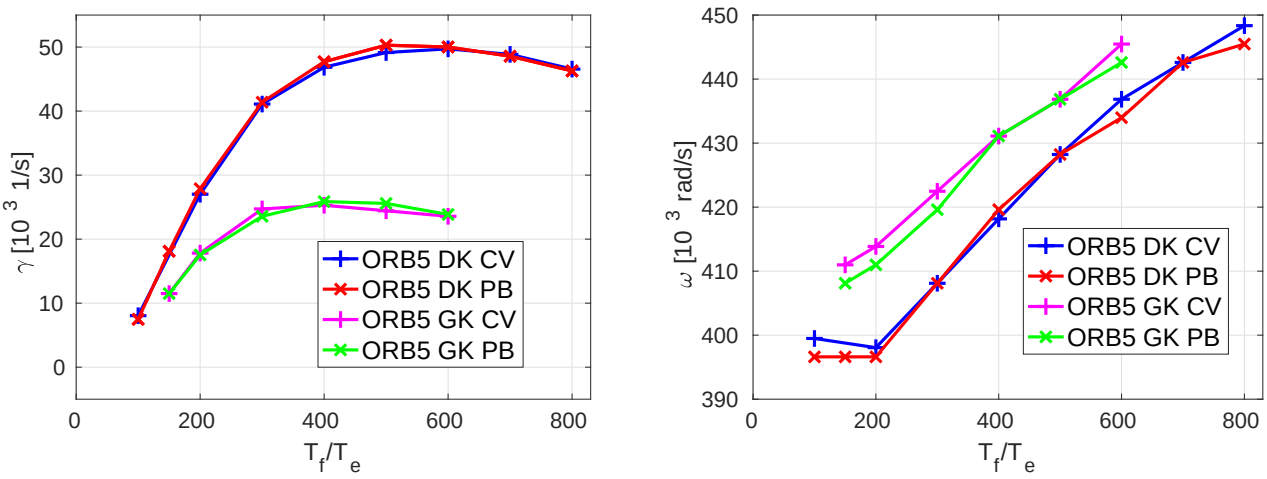

FIG. 1. Dependence of the linear growth rate and the frequency of the TAE instability [19, 20] on the fast-ion temperature. Control-Variate (CV) mitigation [5] is compared with the pullback (PB) mitigation [10]. Drift-kinetic fast ions (DK) are compared with the gyrokinetic (GK) ones.

mode number $n = -6$ and the dominant poloidal mode numbers $m = 10$ and $m = 11$ has been considered in the linear regime. The mode has been studied in tokamak geometry with the small radius $r_\mathrm{a} = 1$ m, the large radius $R_0 = 10$ m, the magnetic field on the axis $B_0 = 3$ T, and the safety factor profile $q(r) = 1.71 + 0.16(r/r_\mathrm{a})^2$, where r is the minor radius of the plasma. The flat background plasma profiles have been chosen with the ion density $n_\mathrm{i} = 2 \times 10^{19}$ m^{-3}, the ion and electron temperatures $T_\mathrm{i} = T_\mathrm{e} = 1$ keV, corresponding to $\beta_\mathrm{bulk} = 2\mu_0(n_\mathrm{i}T_\mathrm{i} + n_\mathrm{e}T_\mathrm{e})/B^2 \approx 0.18$ %. Using the fast-ion parameters of Refs. [19, 20], we obtain the result shown in Fig. 1. Here, the mode growth rate is shown as a function of the fast-ion temperature at the fast-ion density held constant. We compare the simulations using the control-variate approach [5] to the mitigation of the cancellation problem with the simulations using the pullback scheme. One sees that the agreement is very good. This verifies the pullback scheme implementation in ORB5.

For the control-variate simulations, we have used $N_\mathrm{e} = 2 \times 10^7$ electron markers, $N_{im} = 10^7$ ion markers, $N_\mathrm{f} = 10^7$ fast markers, $N_\mathrm{s} = 256$ radial grid points, $N_\theta = 256$ poloidal grid points, and $N_\varphi = 64$ toroidal grid points. The time step is $\omega_\mathrm{ci}\Delta t = 20$. The Fourier filter includes the poloidal modes $9 < m < 12$ and the toroidal mode $n = -6$. Dirichlet boundary conditions for the potentials are set at the axis and at the edge. The ion/electron mass ratio is $m_\mathrm{i}/m_\mathrm{e} = 200$. The initial perturbation of the ion gyrocenter density is localised near the mid-radius, and with mode numbers $m = 10, 11$ and $n = -6$. For the simulations with the pullback mitigation, we have used the same parameters, except the number of markers, which has been set as $N_\mathrm{e} = 5 \times 10^6$ electron markers, $N_\mathrm{i} = 2 \times 10^6$ ion markers, $N_\mathrm{f} = 5 \times 10^6$ fast markers, and the time step, which is $\omega_{ci}\Delta t = 100$. A numerical high-frequency instability rising at outer radii ($s \sim 0.7$) is observed to develop in the simulations with the control variate only, and gyrokinetic fast ions, at large times. In order to postpone the rising time of the instability, it is necessary to increase the number of markers with respect to the values chosen for the simulations with the pullback mitigation.

Now, we consider the benefits of the new pullback scheme in ORB5 simulations. In Fig. 2, the growth rate and the frequency of the TAE mode is shown as a function of the time step used by ORB5. Whereas the control variate mitigation is capable reproducing only the first three points, becoming numerically unstable for larger time steps, the pullback works robustly even for time steps two orders of magnitude larger than the time steps typically used for the electromagnetic simulations with the control variate only. In this simulation, the fast-ion density has been ten times larger (corresponding to 3% particle content) comparing to the standard "ITPA-TAE" benchmark [19, 20]. This makes the simulations faster and more robust.

This improvement in the numerical properties of the code can also be seen in Figs. 3 and 4. Here, we plot the frequency and the growth rate, respectively, as functions of the numerical parameters: the times step and the width of the diagonal Fourier filter [1, 28] used in the ORB5 simulations. Here, we consider the original "ITPA-TAE" [19, 20] parameters again. One sees that the time step needs to be adjusted depending on the number of Fourier modes in the filter (defined by its width) both for the control variate and for the pullback schemes. This requirement is, however, considerably relaxed when the pullback mitigation is used.

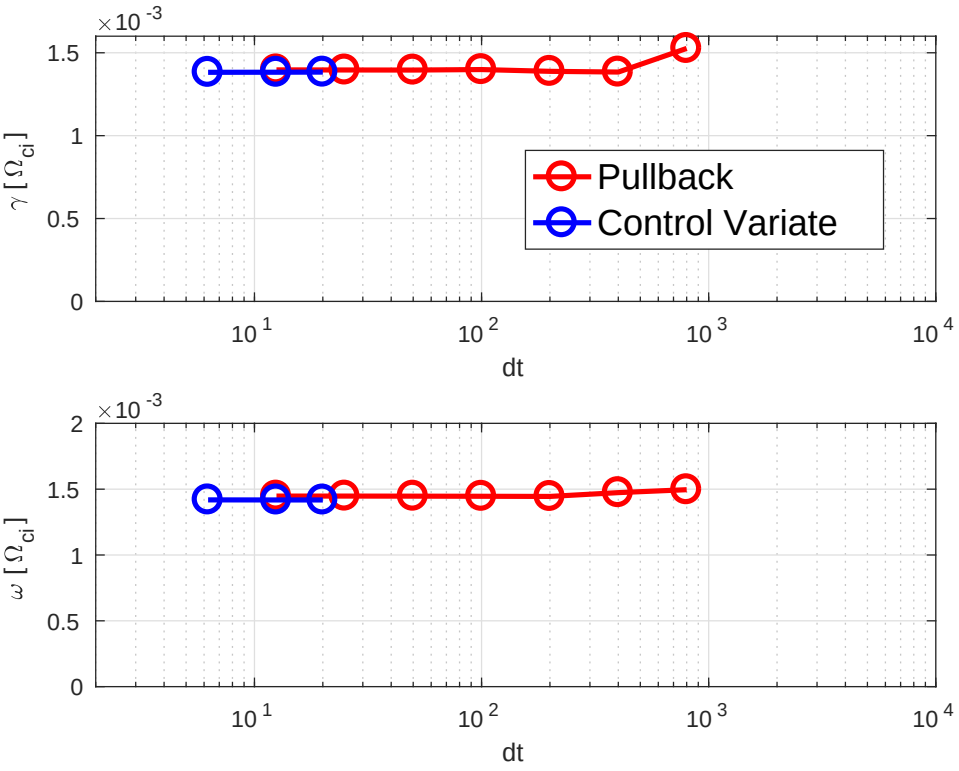

FIG. 2. ITPA-TAE benchmark with increased fast-ion density. The TAE growth rate and the frequency as functions of the time step used by ORB5. The time step can be considerably increased when using the pullback scheme compared to the control variate only, which becomes numerically unstable at larger time steps. The time step is measured in the ion-cyclotron units.

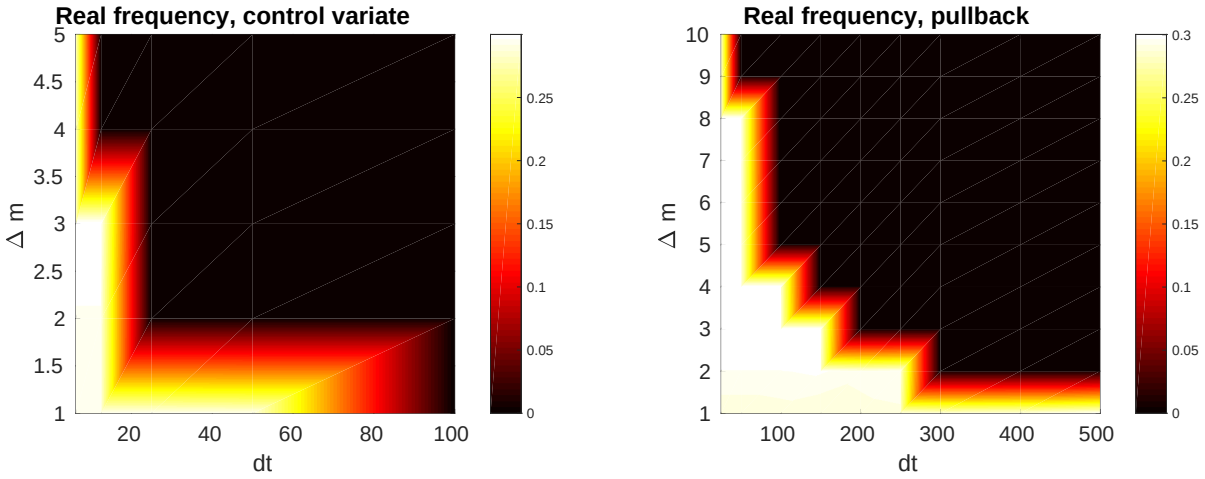

FIG. 3. Real frequency as a function of the diagonal Fourier filter width and the time step. On the left figure, only the control variate has been applied. The time step must be strongly reduced for large filters. On the right figure, the pullback scheme has been used. As a consequence, the time step requirements are considerably relaxed.

B. Internal kink instability

In this Section, we consider an internal kink instability in tokamak geometry. This mode is driven by a combination of ambient parallel current and pressure gradient. In the gyrokinetic model of ORB5, the ambient current must be

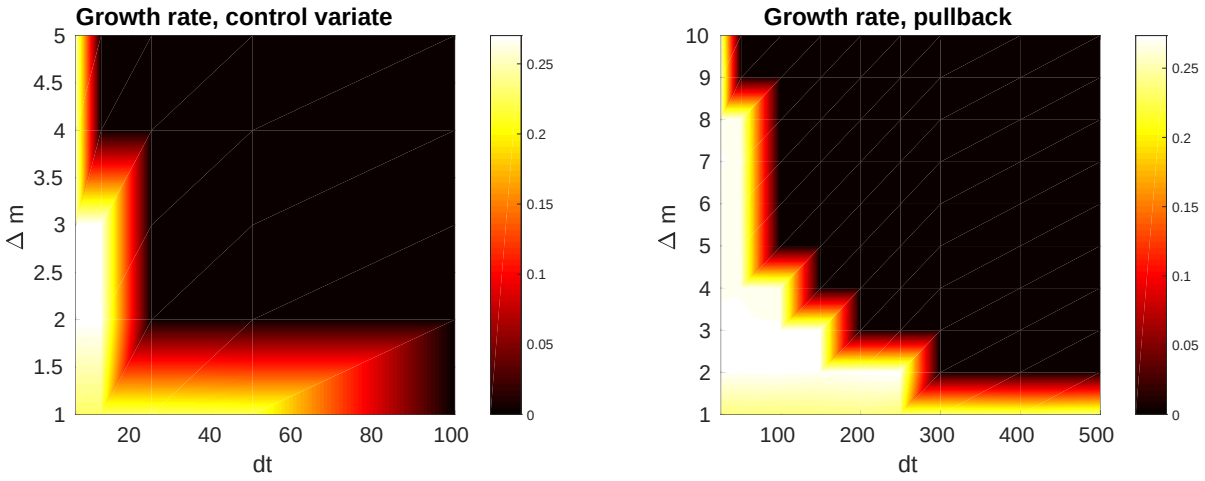

FIG. 4. Growth rate as a function of the diagonal Fourier filter width and the time step. On the left figure, only the control variate is applied. One sees that the time step must be strongly reduced for large filter widths, similar to Fig. 3. On the right figure, the pullback scheme is used. The time step requirements are considerably relaxed.

included as a modification of the background electron distribution function, for example using a shifted Maxwellian:

$$F_{0\mathrm{e}} = n_0 \left(\frac{m_\mathrm{e}}{2\pi T_\mathrm{e}}\right)^{3/2} \exp\left(-\frac{m_\mathrm{e}\varepsilon}{T_\mathrm{e}}\right) \exp\left[-\frac{m_\mathrm{e}u_0(u_0-2v_\parallel)}{2T_\mathrm{e}}\right] \tag{42}$$

written as a function of the energy ε, the parallel velocity $v_\parallel$, the poloidal flux ψ, and the poloidal angle θ:

$$\varepsilon = \frac{v_\parallel^2}{2} + \mu B \ , \quad \mu = \frac{v_\perp^2}{2B} \ , \quad u_0 = \frac{j_{\parallel 0}}{q_\mathrm{e} n_0} \ , \quad j_{\parallel 0}(\psi,\theta) = \frac{1}{\mu_0}\boldsymbol{b}_0(\psi,\theta)\cdot\nabla\times\boldsymbol{B}_0(\psi,\theta) \tag{43}$$

In this paper, we simulate the internal kink instability in the large aspect ratio tokamak geometry and use $j_{\parallel 0}(\psi,\theta=0)$ for simplicity, so that $u_0 = u_0(\psi)$. The spatial derivative is taken at constant ε and $v_\parallel$:

$$\frac{\partial F_{0\mathrm{e}}}{\partial s} = F_{0\mathrm{e}}\left[\frac{n_0'}{n_0} - \left(\frac{3}{2} - \frac{m_\mathrm{e}\varepsilon}{T_\mathrm{e}} - \frac{m_\mathrm{e}u_0(u_0-2v_\parallel)}{2T_\mathrm{e}}\right)\frac{T_\mathrm{e}'}{T_\mathrm{e}} - \frac{m_\mathrm{e}(u_0-v_\parallel)}{T_\mathrm{e}}u_0'\right] \ , \quad n_0' = \frac{\mathrm{d}n_0}{\mathrm{d}\psi} \ , \quad T_\mathrm{e}' = \frac{\mathrm{d}T_\mathrm{e}}{\mathrm{d}\psi} \ , \quad u_0' = \frac{\mathrm{d}u_0}{\mathrm{d}\psi} \tag{44}$$

The parallel-velocity derivative is taken at constant $\boldsymbol{R}$ and ε; the energy derivative is taken at constant $\boldsymbol{R}$ and $v_\parallel$:

$$\frac{\partial F_{0\mathrm{e}}}{\partial v_\parallel} = \frac{m_\mathrm{e}u_0}{T_\mathrm{e}}F_{0\mathrm{e}} \ ; \quad \frac{\partial F_{0\mathrm{e}}}{\partial m_\mathrm{e}\varepsilon} = -\frac{m_\mathrm{e}}{m_\mathrm{e}T_\mathrm{e}}F_{0\mathrm{e}} \tag{45}$$

We consider a tokamak with the minor radius $r_\mathrm{a} = 1$ m, the major radius $R_0 = 10$ m, the magnetic field at the axis $B_0 = 1$ T, flat ion and electron temperatures $T_\mathrm{e} = T_\mathrm{i}$ defined by $L_x = 2r_\mathrm{a}/\rho_\mathrm{s} = 360$ with $\rho_\mathrm{s} = \sqrt{m_\mathrm{i}T_\mathrm{e}}/(eB)$ the sound gyroradius. The safety factor is $q(s) = 0.8(1+s^2)$, the flux surface label $s = \sqrt{\psi/\psi_\mathrm{a}}$ with ψ_a the poloidal flux at the plasma edge. The ambient plasma density profile $n_{0\mathrm{i}}(s) = n_{0\mathrm{e}}(s)$ is given by

$$n_{0\mathrm{e}}(s) = n_0 \exp\left[-\Delta_\mathrm{n}\kappa_\mathrm{n}\tanh\left(\frac{s-s_0}{\Delta_\mathrm{n}}\right)\right] \tag{46}$$

with $\kappa_\mathrm{n} = 3.0$, $s_0 = 0.5$, $\Delta_\mathrm{n} = 0.2$, and n_0 corresponding to $\beta_\mathrm{e} = \mu_0 n_{0\mathrm{e}} T_\mathrm{e}/B^2 = 0.0052$.

The mode evolution is shown in Fig. 5. Here, the simulation using the pullback mitigation is compared to the simulation applying only the control variate (without the pullback mitigation). In both simulations, we use $N_\mathrm{e} = 64\times10^6$ electron markers, $N_\mathrm{i} = 16\times10^6$ ion markers, $N_s = 200$ radial grid points, $N_\theta = 16$ poloidal grid points, and $N_\varphi = 8$ toroidal grid points. The time step is $\omega_{c\mathrm{i}}\Delta t = 10$. The Fourier filter [2] includes the poloidal modes $m \in [-2,2]$ and the toroidal mode $n = 1$ (recall that we consider a large-aspect-ratio tokamak). The ion gyro-average is computed using the adaptive scheme [30], the electrons are drift-kinetic. We initialise our simulations using an initial perturbed distribution function with the poloidal and toroidal mode numbers $m = -1$ and $n = 1$.

In Fig. 5 on the left, one sees that the pullback simulation shows a decay of the shear Alfvén wave continuum and results in a physically-driven internal kink mode developing after the decay phase is completed. In contrast, the simulation using exclusively the control variate becomes immediately numerically unstable. Note that the electrostatic potential reaches very high values within just a few time steps indicating a strong numerical instability at action. Such a pronounced instability is typical for a too large time step. The radial structure of the electrostatic potential developing at the end of each simulation is shown in Fig. 6. Here again, one sees a typical internal kink mode structure resulting from the pullback simulation whereas the control-variate mode structure is unphysical. Further convergence tests with a smaller time step confirm that the control variate scheme becomes unstable for a time step of $\omega_{\rm ci}\Delta t = 10$.

This example shows again that the pullback approach is numerically more robust in terms of the time step compared to the control-variate mitigation. This observation for the kink instability is consistent with the TAE case, shown in Figs. 2 and 3, where the pullback mitigation has performed better than the control variate at larger time steps.

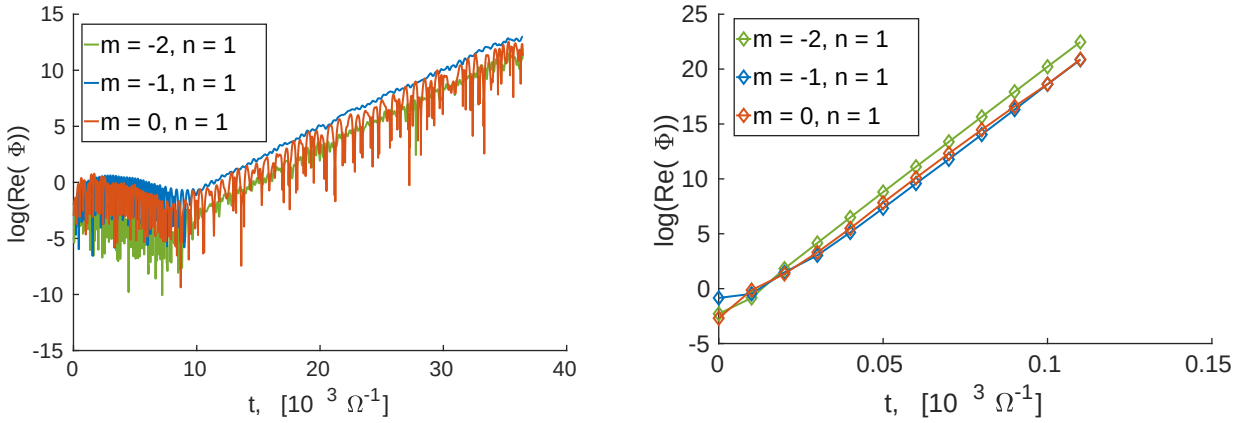

FIG. 5. Mode evolution of the internal kink instability in tokamak geometry. The pullback-scheme simulation on the left is compared to the control-variate simulation with the same set of numerical parameters. Note the different length of the simulations. One sees that the control-variate simulation becomes numerically unstable within a few time steps.

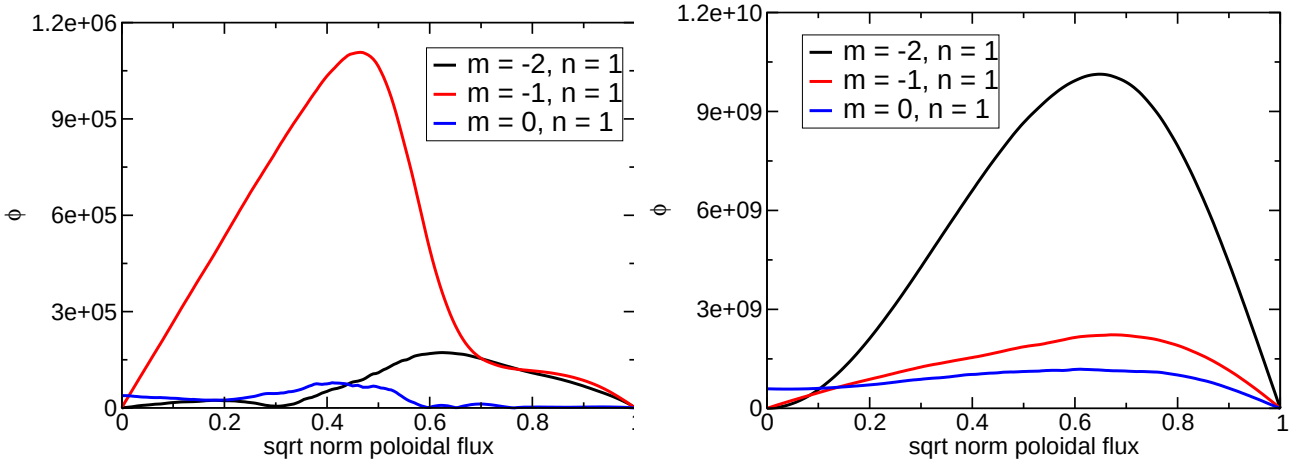

FIG. 6. Mode structure of the internal kink instability in tokamak geometry. On the left, the radial structure of the electrostatic potential resulting from the pullback scheme. On the right, the same electrostatic potential but with only the control variate implemented. All numerical parameters (number of the markers, time step, grid resolution, etc) are identical.

C. Nonlinear simulations

Finally, we compare the pullback scheme with the usual control variate approach in the nonlinear regime. In this case, one should take into account additional nonlinear terms in the mixed-variable equations of motion [11]. The dominant nonlinear contribution is related to

$$\boldsymbol{B}^* = \boldsymbol{B} + \frac{m v_\parallel}{q} \nabla \times \boldsymbol{b} + \nabla \left\langle A_\parallel^{(\mathrm{s})} \right\rangle \times \boldsymbol{b} \tag{47}$$

leading to

$$\boldsymbol{b}^* = \frac{\boldsymbol{B}^*}{B_\parallel^*} = \boldsymbol{b}_0^* + \frac{\nabla \left\langle A_\parallel^{(\mathrm{s})} \right\rangle \times \boldsymbol{b}}{B_\parallel^*} \ , \ \ \boldsymbol{b}_0^* \approx \boldsymbol{b} + \frac{m v_\parallel}{q B_\parallel^*} \nabla \times \boldsymbol{b} \tag{48}$$

The mixed-variable perturbed equations of motion including these nonlinear terms are

$$\dot{\boldsymbol{R}}^{(1)} = \frac{\boldsymbol{b}}{B_\parallel^*} \times \nabla \left\langle \phi - v_\parallel A_\parallel^{(\mathrm{s})} - v_\parallel A_\parallel^{(\mathrm{h})} \right\rangle - \frac{q}{m} \left\langle A_\parallel^{(\mathrm{h})} \right\rangle \left(\boldsymbol{b}_0^* + \frac{\nabla \left\langle A_\parallel^{(\mathrm{s})} \right\rangle \times \boldsymbol{b}}{B_\parallel^*} \right) \tag{49}$$

$$\dot{v}_\parallel^{(1)} = -\frac{q}{m} \left[\boldsymbol{b}^* \cdot \nabla \left\langle \phi - v_\parallel A_\parallel^{(\mathrm{h})} \right\rangle + \frac{\partial}{\partial t} \left\langle A_\parallel^{(\mathrm{s})} \right\rangle \right] - \mu \, \frac{\boldsymbol{b} \times \nabla B}{B_\parallel^*} \cdot \nabla \left\langle A_\parallel^{(\mathrm{s})} \right\rangle \tag{50}$$

Substituting Ohm's law, Eq. (6), we obtain for the parallel velocity

$$\begin{aligned} \dot{v}_\parallel^{(1)} = & - \left(\frac{v_\parallel}{B_\parallel^*} \nabla \times \boldsymbol{b} + \frac{q}{m} \frac{\nabla \left\langle A_\parallel^{(\mathrm{s})} \right\rangle \times \boldsymbol{b}}{B_\parallel^*} \right) \cdot \nabla \left\langle \phi - v_\parallel A_\parallel^{(\mathrm{h})} \right\rangle + \\ & + \frac{q}{m} \, v_\parallel \boldsymbol{b} \cdot \nabla \left\langle A_\parallel^{(\mathrm{h})} \right\rangle - \mu \, \frac{\boldsymbol{b} \times \nabla B}{B_\parallel^*} \cdot \nabla \left\langle A_\parallel^{(\mathrm{s})} \right\rangle \end{aligned} \tag{51}$$

For the perturbed energy, we can write

$$\dot{\varepsilon}^{(1)} = v_\parallel \dot{v}_\parallel^{(1)} + \mu \dot{\boldsymbol{R}}^{(1)} \cdot \nabla B \ , \ \ \varepsilon = \frac{v_\parallel^2}{2} + \mu B \ , \ \ \mu = \frac{v_\perp^2}{2B} \tag{52}$$

$$\begin{aligned} \dot{\varepsilon}^{(1)} = & -\frac{q_s}{m_s} \left[m_s \mu \frac{\boldsymbol{b} \times \nabla B}{q_s B_\parallel^*} + \frac{m_s v_\parallel^2}{q_s B_\parallel^*} (\nabla \times \boldsymbol{b}) + v_\parallel \frac{\nabla \left\langle A_\parallel^{(\mathrm{s})} \right\rangle \times \boldsymbol{b}}{B_\parallel^*} \right] \cdot \nabla \langle \phi \rangle \ + \\ & + \frac{q_s}{m_s} v_\parallel \left[v_\parallel \boldsymbol{b} + m_s \mu \frac{\boldsymbol{b} \times \nabla B}{q_s B_\parallel^*} + \frac{m_s v_\parallel^2}{q_s B_\parallel^*} (\nabla \times \boldsymbol{b}) + v_\parallel \frac{\nabla \left\langle A_\parallel^{(\mathrm{s})} \right\rangle \times \boldsymbol{b}}{B_\parallel^*} \right] \cdot \nabla \langle A_\parallel^{(\mathrm{h})} \rangle \ + \\ & + \frac{q_s}{m_s} \mu B \left[\nabla \cdot \boldsymbol{b} - \frac{m v_\parallel}{q B_\parallel^*} \frac{\nabla \times \boldsymbol{B}}{B^2} \cdot \nabla B - \frac{\nabla \left\langle A_\parallel^{(\mathrm{s})} \right\rangle}{B_\parallel^*} \cdot \frac{\boldsymbol{b} \times \nabla B}{B} \right] \left\langle A_\parallel^{(\mathrm{h})} \right\rangle \end{aligned} \tag{53}$$

Note that the transformation Eq. (10) is perturbative in the field $A_\parallel^{(\mathrm{h})}$. To make it fully nonlinear, we should modify the pullback algorithm to the following [11].

1. At the end of each time step, redefine the magnetic potential splitting, collecting the entire instantaneous value of $A_\parallel(t_i)$ in its 'symplectic part':

$$A_{\parallel(\mathrm{new})}^{(\mathrm{s})}(t_i) = A_\parallel(t_i) = A_{\parallel(\mathrm{old})}^{(\mathrm{s})}(t_i) + A_{\parallel(\mathrm{old})}^{(\mathrm{h})}(t_i) \tag{54}$$

2. As a consequence of the new splitting, Eq. (8), the 'hamiltonian' part of the vector potential must be corrected:

$$A_{\parallel(\mathrm{new})}^{(\mathrm{h})}(t_i) = 0 \tag{55}$$

3. Transform the phase-space coordinates keeping the particle weights constant (this part is modified):

$$v_{\parallel(\mathrm{new})}^{(\mathrm{m})} = v_{\parallel}^{(\mathrm{s})} = v_{\parallel(\mathrm{old})}^{(\mathrm{m})} - \frac{q_s}{m_s}\left\langle A_{\parallel}^{(\mathrm{h})}(t_i)\right\rangle \tag{56}$$

$$f_{1s(\mathrm{new})}^{(\mathrm{m})}\left(v_{\parallel(\mathrm{new})}^{(\mathrm{m})}\right) = f_{1s(\mathrm{old})}^{(\mathrm{m})}\left(v_{\parallel(\mathrm{old})}^{(\mathrm{m})}\right) \tag{57}$$

4. Proceed, explicitly solving the mixed-variable system of equations at the next time step $t_i + \Delta t$ in a usual way, but using Eqs. (56) and (57) as the initial conditions.

In Fig. 7, we consider the nonlinear TAE mode [13] with only the wave-particle nonlinearity kept comparing the three mitigation schemes: the control variate, the linear pullback Eq. (10), and the nonlinear pullback, Eqs. (56) and (57), with the nonlinear terms included in the equations of motion, see Eqs. (49), (50) and (52). Note that in the case of "linear pullback" we still follow the perturbed fast-particle orbits, which makes the simulation itself nonlinear, but we ignore the nonlinear terms in the equations of motion and use the transformation Eq. (10) at the end of every time step. In the case of "nonlinear pullback" all the terms are included in the equations of motion and the nonlinear transformation, Eqs. (56) and (57), is employed.

In our simulations, we use $N_{\mathrm{i}} = 10^7$ ion markers, $N_{\mathrm{e}} = 4 \times 10^7$ electron markers, $N_{\mathrm{f}} = 10^8$ nonlinear fast-ion markers, 256 grid points in the radial and poloidal directions, and 64 grid points in the toroidal direction. The time step is $\omega_{\mathrm{ci}}\Delta t = 20$ for the control variate scheme and $\omega_{\mathrm{ci}}\Delta t = 100$ for the pullback mitigation. We use a reduced mass ration $m_e/m_i = 0.005$ and drift-kinetic fast ions. One sees that both the saturation levels and the linear evolution agree very well in Fig. 7 for all the schemes. This verifies the new pullback implementation in ORB5 also nonlinearly. Interestingly, the discrepancy between the "linear pullback" and "nonlinear pullback" in terms of the saturation level was larger for the tearing mode [11] where the electron nonlinearity was important. Here, we see that this difference is negligible for the fast-particle nonlinearity. Thus, the original pullback scheme and the mixed-variable equations described in Sec. II can safely be used for the Alfvénic simulations where the fast-ion nonlinearity is dominant.

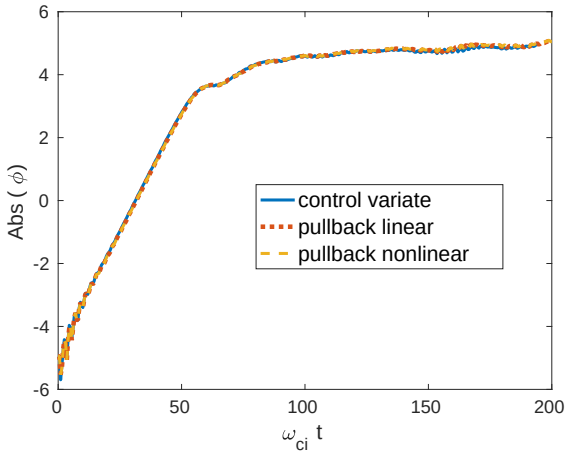

FIG. 7. Nonlinear simulations with drift-kinetic fast ions. Control-variate mitigation is compared with the linear and nonlinear pullback schemes, see Eqs. (10) and (56) respectively. Note that, not only the linear growth rate, but also the nonlinear saturation level agrees well with and without the pullback scheme.

V. CONCLUSIONS

The pullback scheme has been implemented in ORB5. The solver modifications needed for the pullback scheme implementation have been described. The new scheme has been verified using the ITPA-TAE benchmark [19, 20] both in the linear and nonlinear regimes. A considerable improvement of the code efficiency has been observed. Also, the efficiency of the pullback mitigation in ORB5 has been demonstrated using the internal kink mode in tokamak geometry. To our knowledge, internal kink mode simulations in tokamak geometry have not been reported previously for global gyrokinetic particle-in-cell codes, such as ORB5, using realistic values for the plasma β.

In the outlook, ORB5 provides a unified framework which includes electromagnetic drift-wave turbulence, zonal flows and GAMs, fast particles, shear Alfvén waves (TAEs, BAEs, etc), and MHD activity (tearing mode, internal kink instability) in axisymmetric tokamak geometry. This represents a vast field for future research.

Acknowledgements We acknowledge P. Helander, E. Sonnendrücker, F. Jenko, S. Günter, F. Zonca, and Ph. Lauber for their support. Numerical simulations were performed on the Marconi supercomputer within the framework of the OrbZONE and OrbFAST projects. This work has been carried out within the framework of the EUROfusion Consortium and has received funding from the Euratom research and training program 2014–2018 under Grant Agreement No. 633053, for the CfP-AWP17-ENR-MPG-01 (2017/2018) project on "Nonlinear interaction of Alfvénic and turbulent fluctuations in burning plasmas (NAT)". The views and opinions expressed herein do not necessarily reflect those of the European Commission.

[1] S. Jolliet, A. Bottino, P. Angelino, R. Hatzky, T. M. Tran, B. F. Mcmillan, O. Sauter, K. Appert, Y. Idomura, and L. Villard, Comp. Phys. Commun. **177**, 409 (2007).
[2] B. F. McMillan, S. Jolliet, T. M. Tran, L. Villard, A. Bottino, and P. Angelino, Phys. Plasmas **15**, 052308 (2008), https://doi.org/10.1063/1.2921792.
[3] Y. Chen and S. Parker, Phys. Plasmas **8**, 2095 (2001).
[4] A. Mishchenko, R. Hatzky, and A. Könies, Phys. Plasmas **11**, 5480 (2004).
[5] R. Hatzky, A. Könies, and A. Mishchenko, J. Comp. Phys. **225**, 568 (2007).
[6] A. Bottino, T. Vernay, B. Scott, S. Brunner, R. Hatzky, S. Jolliet, B. F. McMillan, T. M. Tran, and L. Villard, Plasma Physics and Controlled Fusion **53**, 124027 (2011).
[7] A. Biancalani, A. Bottino, S. Briguglio, A. Könies, Ph. Lauber, A. Mishchenko, E. Poli, B. D. Scott, and F. Zonca, Phys. Plasmas **23**, 012108 (2016).
[8] A. Biancalani, A. Bottino, M. Cole, C. Di Troia, Ph. Lauber, A. Mishchenko, B. Scott and F. Zonca, Plasma Phys. Controlled Fusion **59**, 054004 (2017).
[9] A. Mishchenko, M. Cole, R. Kleiber, and A. Könies, Phys. Plasmas **21**, 052113 (2014).
[10] A. Mishchenko, A. Könies, R. Kleiber, and M. Cole, Phys. Plasmas **21**, 092110 (2014).
[11] R. Kleiber, R. Hatzky, A. Könies, A. Mishchenko, and E. Sonnendrücker, Phys. Plasmas **23**, 032501 (2016).
[12] A. Mishchenko, A. Bottino, R. Hatzky, E. Sonnendrcker, R. Kleiber, and A. Könies, Phys. Plasmas **24**, 081206 (2017), https://doi.org/10.1063/1.4997540.
[13] M. Cole, A. Biancalani, A. Bottino, R. Kleiber, A. Könies, and A. Mishchenko, Phys. Plasmas **24**, 022508 (2017).
[14] M. Cole, M. Borchardt, R. Kleiber, A. Könies, and A. Mishchenko, Phys. Plasmas **25**, 012301 (2018), https://doi.org/10.1063/1.5002584.
[15] J. Bao, D. Liu, and Z. Lin, Phys. Plasmas **24**, 102516 (2017), https://doi.org/10.1063/1.4995455.
[16] J. Bao, Z. Lin, and Z. X. Lu, Phys. Plasmas **25**, 022515 (2018), https://doi.org/10.1063/1.5016432.
[17] C. Z. Cheng, L. Chen, and M. S. Chance, Ann. Phys. **161**, 21 (1985).
[18] L. Chen and F. Zonca, Rev. Mod. Phys. **88**, 015008 (2016).
[19] A. Könies, S. Briguglio, N. Gorelenkov, T. Fehér, M. Isaev, P. Lauber, A. Mishchenko, D. A. Spong, Y. Todo, W. A. Cooper, R. Hatzky, R. Kleiber, M. Borchardt, G. Vlad, ITPA EP TG, in *Proc. of 24th Fusion Energy Conf.* (IAEA, Vienna, 2012).
[20] A. Könies, S. Briguglio, N. Gorelenkov, T. Feher, G. Y. Fu, M. Isaev, P. Lauber, A. Mishchenko, D. A. Spong, W. A. Cooper, R. Hatzky, R. Kleiber, A. Biancalani, and A. Bottino, Nucl. Fusion , accepted (2018).
[21] V. D. Shafranov, Zh. Tekh. Fiz. **40**, 241 (1970).
[22] H. Naitou, K. Tsuda, W. W. Lee, and R. D. Sydora, Phys. Plasmas **2**, 4257 (1995).
[23] H. Naitou, K. Kobayashi, H. Hashimoto, S. Tokuda, and M. Yagi, J. Plasma Fusion Res. Series **8**, 1158 (2009).
[24] A. Mishchenko and A. Zocco, Phys. Plasmas **19**, 122104 (2012).
[25] A. J. Brizard and T. S. Hahm, Reviews of Modern Physics **79**, 421 (2007).
[26] A. Bottino and E. Sonnendrücker, Journal of Plasma Physics **81**, 435810501 (2015).
[27] N. Tronko, A. Bottino, and E. Sonnendrücker, Phys. Plasmas **23**, 082505 (2016), https://doi.org/10.1063/1.4960039.
[28] B. F. McMillan, S. Jolliet, A. Bottino, P. Angelino, T. M. Tran, and L. Villard, Comp. Phys. Commun. **181**, 715 (2010).
[29] K. Höllig, *Finite Element Methods with B-Splines* (Society for Industrial and Applied Mathematics, Philadelphia, 2003).
[30] R. Hatzky, T. M. Tran, A. Könies, R. Kleiber, and S. J. Allfrey, Phys. Plasmas **9**, 898 (2002).